

Spin-Selective and Wavelength-Selective Demultiplexing Based on Waveguide-Integrated All-Dielectric Metasurfaces

Yuebian Zhang, Zhancheng Li, Wenwei Liu, Zhi Li, Hua Cheng,* Shuqi Chen,* and Jianguo Tian

A novel approach for the design of a spin-selective directional coupler and spin-selective wavelength demultiplexing device by integrating an all-dielectric metasurface into a silicon nitride waveguide is proposed and demonstrated. Taking advantage of the intrinsic chirality of the electromagnetic field inside the waveguide, the propagation direction of the excited waveguide mode can be easily controlled by the spin and wavelength of the incident light. The coupling efficiency of the spin-selective directional coupler toward one side can reach $\approx 51.6\%$ at 1836 nm. In addition, the working wavelengths, coupling efficiency, peak width, and mode type can be easily tailored by adjusting the geometric parameters of the waveguide and the antenna arrays. This study may provide a further step in the development of photonic integrated circuits, integrated quantum optics, chiral optics, and high-bit-rate telecommunication applications.

Nanophotonic waveguides play a vital role in photonic integrated circuits and they represent an attractive platform for novel on-chip optical applications such as integrated quantum optics,^[1,2] optical information processing,^[3] and photon switching.^[4] The ability to detect and control multiple degrees of freedom simultaneously is central to efficient use of photons in a waveguide. For example, to satisfy the increasing demands for high capacity in optical interconnects, multiplexing and demultiplexing technologies that use different properties of light have been proposed, e.g., wavelength (de)multiplexing,^[5] polarization (de)multiplexing,^[6] and mode (de)multiplexing.^[3,7] Over the past decade, research interest in (de)multiplexing technologies has extended from a single degree of freedom to multiple degrees of freedom, e.g., simultaneous mode- and polarization-multiplexing^[8,9] or simultaneous


mode- and wavelength-multiplexing.^[10] Unfortunately, waveguide (de)multiplexing technology remains limited in terms of the manner of coupling, which is generally manifest as horizontal coupling based on fibers and microcavities.^[3,7] However, coupling of vertical free-space light to a waveguide is desirable in many applications such as novel types of solar cell, photo detectors, and advanced lasers.^[11,12]

One way to couple free-space light into a waveguide is to integrate nanoantennas with the waveguides.^[13–16] A nanoantenna provides the means to downscale photonic integrated circuits, and it can act as an ideal bridge linking free-space waves and guided waves for their unique resonance and scattering properties. It has been

demonstrated that waveguide-hybridized Yagi–Uda antennas could realize directional in-coupling of free-space waves and directional out-coupling of guided waves.^[13] By tailoring the radiation phases of a gold nanodisk and a nanoslit integrated onto a dielectric waveguide, a linearly polarized beam can be routed in opposite directions at two different wavelengths.^[14] Recently, Guo et al. demonstrated that waveguide-integrated nanoantennas can realize mode-selective polarization (de)multiplexing.^[16] However, these earlier studies were mainly based on the scattering of several plasmonic nanostructures and thus the coupling efficiencies were very low.^[13–16] One way to address this problem is to use phase-gradient metasurfaces, which are 2D nanostructure arrays that can control the wavefront of light at will.^[17] Recently, it was reported that phase-gradient metasurfaces could be integrated into waveguides to realize asymmetric optical power transmission, polarization rotation, and mode conversion.^[18] The effective wavevector introduced by nanoantenna arrays can also be used to relax the phase-matching requirement in on-chip nonlinear wavelength conversion.^[19] Based on the phase-gradient metasurface, a hybrid unidirectional meta-coupler for vertical incidence to a waveguide at telecoms wavelength has been demonstrated.^[20] The simulated coupling efficiencies can reach about 70%; however, this coupler only works for linearly polarized beams and it cannot realize wavelength demultiplexing.

Spin angular momentum (SAM) is regarded as one of the most significant properties of electromagnetic fields and it is vital in chiral optics. In free space, the SAM of light is associated with its circular polarization and is parallel to the propagation direction. However, because of the strong transverse confinement of the guided photons, their polarization states

Dr. Y. Zhang, Dr. Z. Li, Dr. W. Liu, Dr. Z. Li, Prof. H. Cheng, Prof. S. Chen, Prof. J. Tian
The Key Laboratory of Weak Light Nonlinear Photonics
Ministry of Education
School of Physics and TEDA Institute of Applied Physics
Nankai University
Tianjin 300071, China
E-mail: hcheng@nankai.edu.cn; schen@nankai.edu.cn
Prof. H. Cheng, Prof. S. Chen, Prof. J. Tian
The Collaborative Innovation Center of Extreme Optics
Shanxi University
Taiyuan, Shanxi 030006, China

 The ORCID identification number(s) for the author(s) of this article can be found under <https://doi.org/10.1002/adom.201801273>.

DOI: 10.1002/adom.201801273

are associated with the distribution of mode fields and the propagation direction of light in the waveguide.^[21,22] It was reported that another type of SAM called transverse SAM exists in a waveguide, which is orthogonal to the propagation direction.^[23,24] More interestingly, the transverse SAM of evanescent and guided waves leads to the phenomenon of spin-momentum locking via spin-orbit coupling, which is a phenomenon whereby the direction of momentum fundamentally locks the spin of the wave.^[25–27] When a circularly polarized dipole emitter or a scattering antenna is placed in an evanescent-wave region showing local circular polarization, the guided mode can be excited unidirectionally.^[22,24,27,28] This phenomenon inspires us to integrate phase-gradient metasurfaces with waveguides to realize high-efficiency spin-selective directional coupling of free-space waves. More importantly, the multimode behavior of a waveguide results in different spin-orbit coupling properties for different guided modes, making it possible to realize spin-selective wavelength demultiplexing. Although several works have demonstrated spin-dependent directional coupling for slab and rectangular waveguides based on geometric metasurfaces,^[29,30] they did not exploit the spin-momentum locking effect and thus could not realize wavelength demultiplexing.

In this article, we propose and demonstrate a novel approach for the design of a spin-selective directional coupler and spin-selective wavelength demultiplexing device by integrating all-dielectric metasurfaces into silicon nitride waveguides. First, we demonstrate a spin-selective directional coupler that can couple free-space light into a waveguide at one wavelength, where the propagation direction of the guided wave can be controlled by the spin of the incident light. The coupling efficiency of the spin-selective directional coupler toward one side can reach about 51.6% at 1836 nm. Then, we study the basic physical mechanisms and properties of the spin-selective directional coupler. We demonstrate that the properties of the proposed devices can be tailored easily by adjusting different geometric parameters. Finally, we demonstrate a spin-selective wavelength demultiplexing device that can convert incident light to different waveguide modes propagating to different directions at different wavelengths. Our work represents the first attempt to realize spin-selective wavelength demultiplexing using waveguide-integrated metasurfaces. This study could provide a further step in the development of photonic integrated circuits, integrated quantum optics, chiral optics, and high-bit-rate telecommunication applications.

The designed spin-selective wavelength demultiplexing device is shown in **Figure 1**. It comprises a SiO₂ substrate, Si₃N₄ waveguide, and three rows of silicon nanopillar arrays. The waveguide has width W and thickness t . The major axis, minor axis, and height of each elliptical silicon nanopillar are a , b , and h , respectively. The distance between two adjacent nanopillars along the x -axis is P . The nanopillars are arranged alternately with orientation angle $\theta = 0^\circ/90^\circ$. The y -coordinates of the nanopillar arrays are s_1 , s_2 , and s_3 . The proposed structure can be fabricated by using low-pressure chemical vapor deposition and e-beam lithography, as reported in ref. [18]. The finite element method-based commercial software COMSOL Multiphysics^[31] was used to optimize the geometric parameters of the unit cell, and other numerical simulations were conducted using a finite difference time-domain approach based on the Lumerical Solutions commercial software package. Two

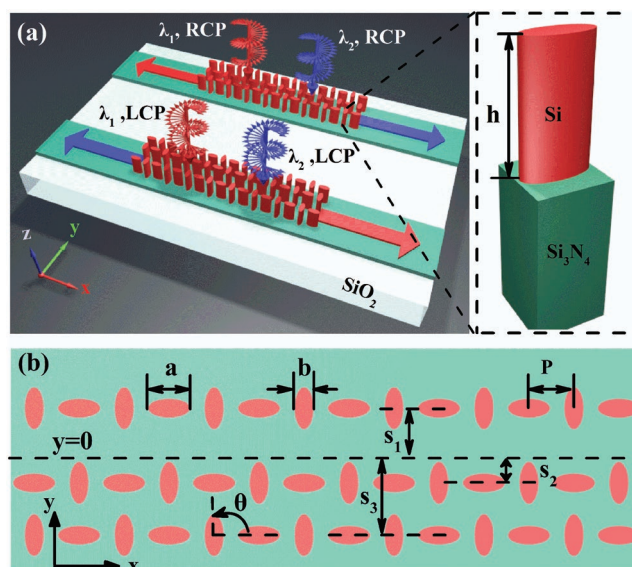


Figure 1. a) Schematic of the spin-selective wavelength demultiplexing device. The device couples circular-polarized light of different wavelengths into different directions in the underlying waveguide. At a fixed wavelength, the direction of light flow in the waveguide can be flipped when the chirality of the incident light is reversed. The inset shows a unit cell of the dielectric resonator. b) Plan view and geometric parameters of the silicon nanostructures.

total-field-scattered-field sources of the same width as the waveguide were used to simulate the incident circular-polarized plane wave on the antennas. Two power monitors were located at $x = \pm 29 \mu\text{m}$ to record the power through the waveguide. The transmission efficiencies (coupling efficiencies) of the spin-selective devices are defined as the ratio of the power recorded by the power monitors to the incident power^[14]: $\eta = P_{\text{monitor}}/P_{\text{in}}$. The optical constants of amorphous silicon and Si₃N₄ were taken from refs. [32] and [33], respectively. The refractive index of the SiO₂ substrate is 1.44.

To construct the waveguide-integrated metasurface, we first designed an elliptical silicon nanopillar arrays that can act as an imperfect half-wave plate with reasonably high efficiency. The optimized geometric parameters of the periodic nanopillars are $P_x = P_y = P = 630 \text{ nm}$, $t = 1000 \text{ nm}$, $a = 560 \text{ nm}$, and $b = 250 \text{ nm}$. The transmission spectra of the unit cell are shown in **Figure 2a**. It can be seen that most of the left-handed circular polarized (LCP) incident light can be converted to right-handed circular polarized (RCP) light over a broad range of wavelength. According to the Pancharatnam–Berry phase (P–B phase) theory, the phase of the converted RCP light can be changed by spatially rotating the unit cell.^[17] The phase change can be written as $\Phi = 2\sigma\theta$, where $\sigma = \pm 1$ represents either the LCP or RCP light. As shown in Figure 2b, the phase of the transmitted RCP light increases linearly with orientation angle θ at 1836 nm. In addition, the transmission of the RCP light can reach about 80% and it is almost independent of orientation angle. To couple the free-space light into the waveguide, the phase-matching condition between the coupler and the waveguide mode must be satisfied. This condition can be written as $n_{\text{eff}} = \frac{\lambda}{2\pi} \cdot \frac{|\Delta\Phi|}{P}$, where n_{eff} is the effective refractive index of the waveguide mode, λ is the wavelength in free space, and

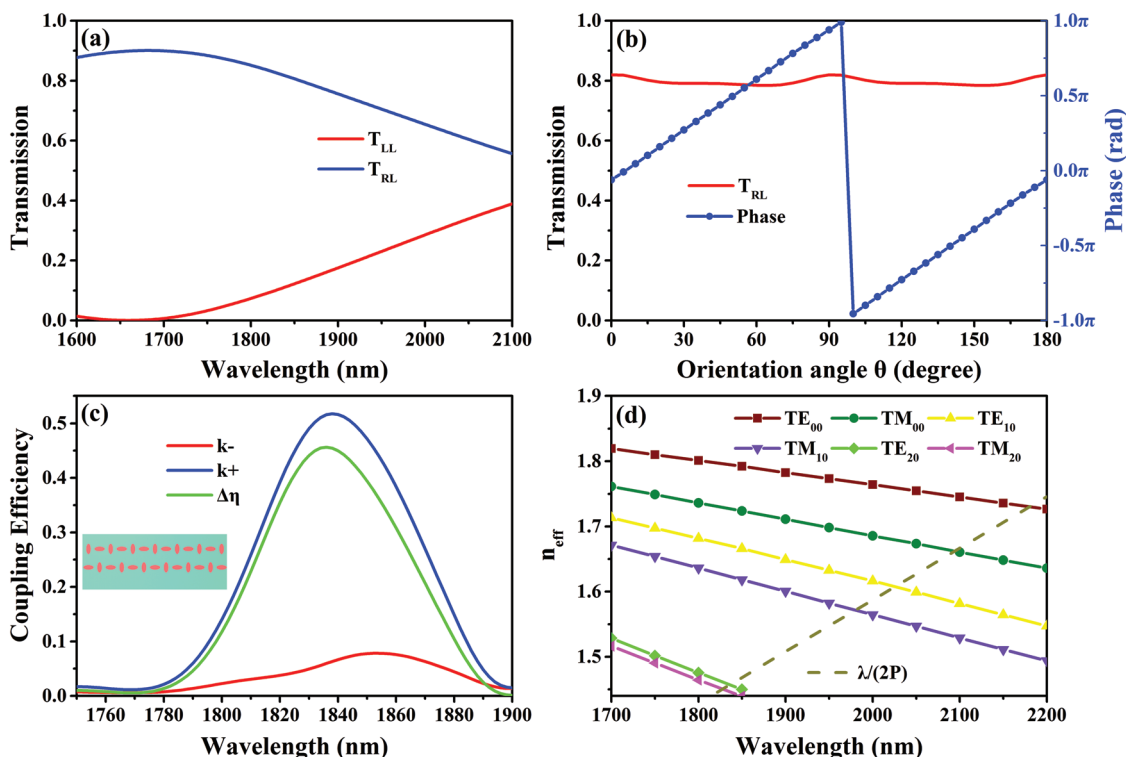


Figure 2. a) Transmission spectra of the metasurface composed of periodic elliptical silicon nanopillars for LCP incidence. The geometric parameters of the nanopillars are $P = 630$ nm, $t = 1000$ nm, $a = 560$ nm, $b = 250$ nm. b) Transmission and phase of the silicon nanopillar arrays as a function of orientation angle θ at wavelength 1836 nm. c) Coupling efficiency spectra toward different sides of the waveguide and their difference $\Delta\eta$ for the spin-selective directional coupler for RCP incidence. $k+/k-$ correspond to light propagating along the $+x/-x$ direction. Inset shows the top view of the silicon nanoarrays. d) Effective indices of the optical modes in the waveguide as a function of wavelength. The waveguide width is 2300 nm and its thickness is 800 nm.

$\Delta\Phi$ is the phase difference between two adjacent nanopillars along the x -axis. In our design, we arranged the nanopillars alternately with orientation angle $\theta = 0^\circ/90^\circ$. Consequently, $\Delta\Phi = \pm\pi$ can be achieved and the phase-matching condition becomes $n_{\text{eff}} = \frac{\lambda}{2P}$. It should be noted that, unlike the unidirectional coupler based on the P–B phase demonstrated in ref. [30], which relied on a unidirectional phase gradient, our coupler can couple the LCP (RCP) light into two directions if the nanopillar arrays lie in the central axis of the waveguide.

To demonstrate the principle of our spin-selective directional coupler, we designed a spin-selective directional coupler containing only two rows of antenna arrays. Both rows of antenna arrays contained 35 elliptical silicon nanopillars. The y -coordinates of the nanopillar arrays are $s_1 = 700$ nm and $s_2 = -300$ nm. The geometric parameters of the waveguide are $W = 2300$ nm and $t = 800$ nm. Figure 2c shows the coupling efficiency spectra toward different sides of the waveguide for RCP incidence. For RCP incident light around 1836 nm, it can be seen that most of the power scattered from the antenna arrays is coupled to the right side ($+x$ direction) of the waveguide. The coupling efficiency toward the right side can reach about 51.6% at 1836 nm, which is much larger than previously reported.^[30] In addition, we calculated the coupling efficiency difference $\Delta\eta = \eta_{k+} - \eta_{k-}$ between the two directions, which could reach about 45.6% at 1836 nm. To get insight into the nature of the directional excited waveguide mode, we calculated the effective indices of

the optical modes in the waveguide as a function of wavelength. The dashed line in Figure 2d shows the value of $\lambda/(2P)$ at each wavelength. Results show that only the TE_{20} and TM_{20} modes (we adopt the nomenclature of modes in the dielectric waveguides demonstrated in ref. [18]) satisfy the phase-matching condition in the range 1750–1900 nm, which agrees well with the position of peak coupling efficiency. This indicates that the excited modes are composed primarily of the TE_{20} and TM_{20} modes.

To further study the directional excited waveguide mode, we plot the electric field amplitude distribution $|\vec{E}|$ in the x - y plane bisecting the waveguide for RCP and LCP incidence at 1836 nm in Figure 3a and 3c, respectively. For RCP incidence, a waveguide mode that has three antinodes along the y -axis is excited and routed to the $+x$ direction, which is in accord with the field amplitude distribution of the TE_{20} and TM_{20} modes. However, when the chirality of the incident light is reversed, the light flowing in the waveguide is flipped to the opposite direction. This directionality originates from the internal intrinsic chirality of the electromagnetic field inside the waveguide.^[22] A waveguide can support both longitudinal and transverse field components (E_x and E_y) and it can permit the transfer of in-plane circular polarization ($E_x \pm iE_y$). Some chiral points exist along the y -axis where the local electromagnetic field vectors are circular polarization. The rotational direction of the electric field at chiral points is dependent on the position, mode field distribution, and propagation direction of the guided waves.

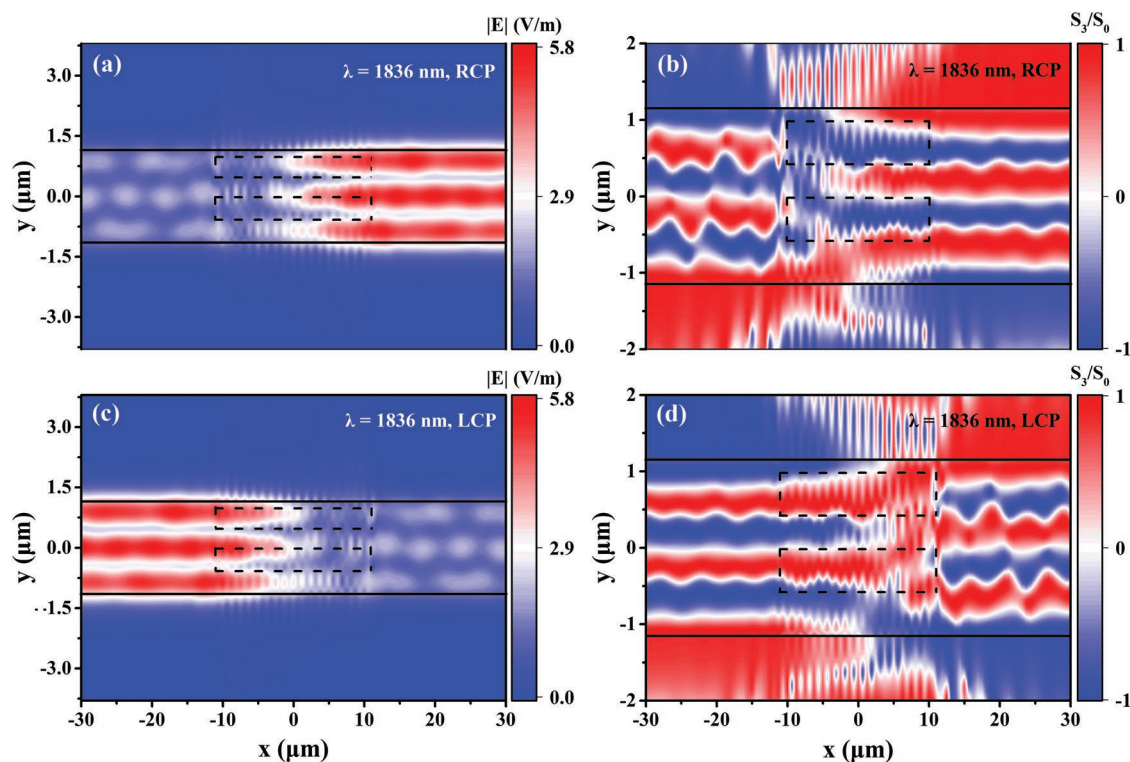


Figure 3. a) Electric field amplitude distribution $|\vec{E}|$ and b) Stokes parameter S_3/S_0 in the x - y plane bisecting the waveguide for RCP incidence at 1836 nm. c) Electric field amplitude distribution $|\vec{E}|$ and d) Stokes parameter S_3/S_0 in the x - y plane bisecting the waveguide for LCP incidence at 1836 nm. Black dashed lines in the four panels indicate locations of antenna arrays.

If an emitter or an antenna emitting circularly polarized light is placed at the chiral points, the light will be coupled into the waveguide unidirectionally. This condition, which realizes the spin-momentum locking effect in the waveguide, can be called the mode field-matching condition. To further demonstrate the origin of the spin-selective directional coupling, we plot the Stokes parameters S_3/S_0 for the mode fields in the x - y plane bisecting the waveguide for RCP and LCP incidence at 1836 nm in Figure 3b and 3d, respectively. The Stokes parameters are defined as $S_0 = |E_x|^2 + |E_y|^2$ and $S_3 = 2\text{Im}\{E_x^* E_y\}$. A value of S_3/S_0 close to +1 or -1 represents nearly perfect in-plane RCP or LCP light, respectively. For RCP and LCP incidence, the positions of the chiral points (where $S_3/S_0 = \pm 1$) are almost the same. The differences between them are mainly due to the difference in intensity of the electromagnetic field and the scattering of the nanoantennas. In addition, the rotational directions (chirality) of the electric field are opposite for light propagating in different directions. Moreover, the nanopillar arrays are located approximately at the chiral points. For RCP or LCP incidence, the cross-polarized light scattered by the nanoantenna arrays is mainly coupled to the mode whose local polarization is LCP or RCP, respectively. This phenomenon can be explained by Fermi's golden rule.^[27,28] According to this rule, the coupling efficiency between a dipole source and a waveguide mode is proportional to the similarity between the dipole moments and the mode fields in the waveguide. Consequently, for a specified waveguide mode, the coupling efficiency and propagation direction of the guided waves are dependent on the position of the nanoantenna arrays and the

polarization of the incident light. It should be noted, because only the cross-polarized lights have the needed P-B phase, the coupling efficiencies of the spin-selective devices are also dependent on the polarization conversion efficiencies of the silicon nanopillar arrays. To obtain a relatively high efficiency, the geometric parameters of the silicon nanopillars and the positions of the nanoantenna arrays must be optimized simultaneously.

To study the dependence of the directional coupling on the position of the nanoantenna arrays, we simulated the coupling efficiency spectra toward different sides of the waveguide as a function of array position s for RCP incidence. Only one antenna array row comprising 35 antennas was used in the simulation and the other geometric parameters were the same as those used in producing Figure 2c. As shown in Figure 4a, when the antenna array is located at the center of the waveguide ($s = 0$), incident light is coupled into the waveguide with the same coupling efficiency for both directions and there is no spin-selective directional coupling. However, when the antenna array is displaced from the center of the waveguide, the coupling efficiency toward either side of the waveguide becomes different. At some points, light in the waveguide is routed mainly to the $+x$ direction, while at other points, light is routed mainly to the $-x$ direction. The positions of the coupling efficiency peaks correspond to the chiral points of the waveguide. To show the directional coupling more clearly, we plot the coupling efficiency difference $\Delta\eta$ as a function of array position s in Figure 4b. It can be seen that the coupling efficiency difference can reach the maximum value when $s = -240$ nm or $s = 690$ nm.

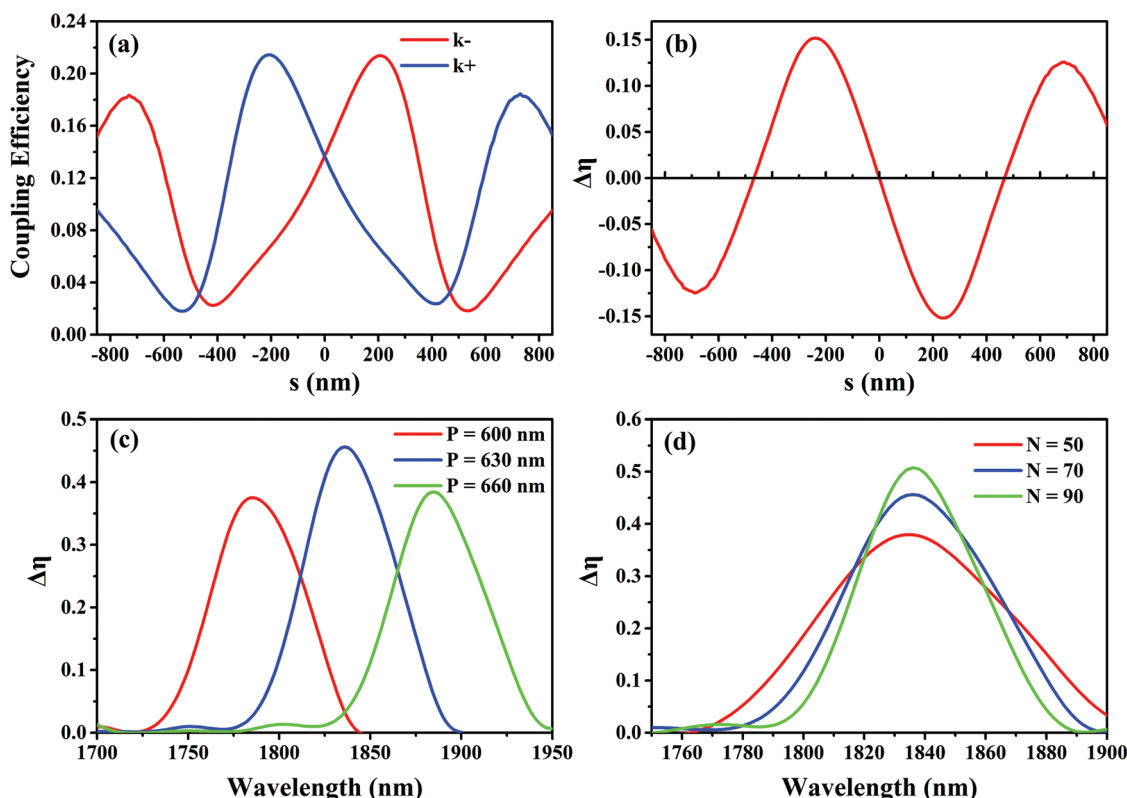


Figure 4. a) Coupling efficiency spectra toward different sides of the waveguide as a function of array position s for RCP incidence at 1836 nm. b) Coupling efficiency difference $\Delta\eta$ as a function of array position s . Only one antenna array row comprising 35 antennas was used in (a) and (b). c) Coupling efficiency difference $\Delta\eta$ for different antenna period P . d) Coupling efficiency difference $\Delta\eta$ for different numbers of antennas N . The structure used in (c) and (d) contained two rows of antenna arrays.

When $s = 240$ nm or $s = -690$ nm, the coupling efficiency difference will reverse the sign, which indicates directional propagation toward the $-x$ direction. Therefore, we can control the propagation direction of the guided waves by adjusting the array position. To study the dependence of the coupling efficiency spectra on the distance between nanopillars along the x -axis, we varied parameter P of the spin-selective directional coupler and kept the other parameters unchanged (Figure 4c). It can be seen that there is a redshift of the working wavelength with increasing P . This phenomenon can be explained by the phase-matching condition. With increasing P , the wavelength that satisfies the phase-matching condition will be redshifted. In addition, the peak value of the coupling efficiency difference $\Delta\eta$ reaches the maximum when P is about 630 nm. We also studied the impact of the number of antennas N on the coupling efficiency difference $\Delta\eta$ in Figure 4d. When the number of antennas increases, the peak position of the coupling efficiency difference $\Delta\eta$ remains unchanged, while the value of the peak increases. In addition, the peak width decreases with increasing N . For the designed directional coupler structure, two rows of antenna arrays, each of which comprised 35 antennas, were used to obtain a moderate peak width. Therefore, the properties of the spin-selective directional coupler can be tailored easily by adjusting different geometric parameters.

Given that different waveguide modes have different mode field distributions and thus have different chiral points, it is

possible to design a spin-selective wavelength demultiplexing device that can couple incident light to different waveguide modes and different propagation directions at different wavelengths. To design this device, the waveguide and the nanoantenna arrays should be adjusted to satisfy both the phase-matching condition and the mode field-matching condition simultaneously at two different wavelengths. In addition, the chirality for one specified direction around the nanoantenna arrays should be opposite for the two wavelengths. Our spin-selective wavelength demultiplexing device contains three rows of antenna arrays (as shown in Figure 1). Each row of antenna arrays contains 35 elliptical silicon nanopillars. The y -coordinates of the nanopillar arrays are $s_1 = 700$ nm, $s_2 = -250$ nm, and $s_3 = -1200$ nm. The geometric parameters of the waveguide are $W = 3000$ nm and $t = 800$ nm. Figure 5a shows the coupling efficiency spectra toward different sides of the waveguide for RCP incidence. It can be seen that incident light at about 1810 nm is routed to the $-x$ direction, while incident light at about 1926 and 1970 nm is routed to the $+x$ direction. The coupling efficiencies toward the left and right sides can reach 45.2% at 1810 nm and 37.3% at 1970 nm, respectively. The coupling efficiency difference $\Delta\eta$ between the two sides of the waveguide at 1810 and 1970 nm are -38.8% and 30.9% , respectively. To identify the modes in the waveguide at each wavelength, we decomposed the coupling efficiency spectra into different waveguide modes, as shown in Figure 5c,d.

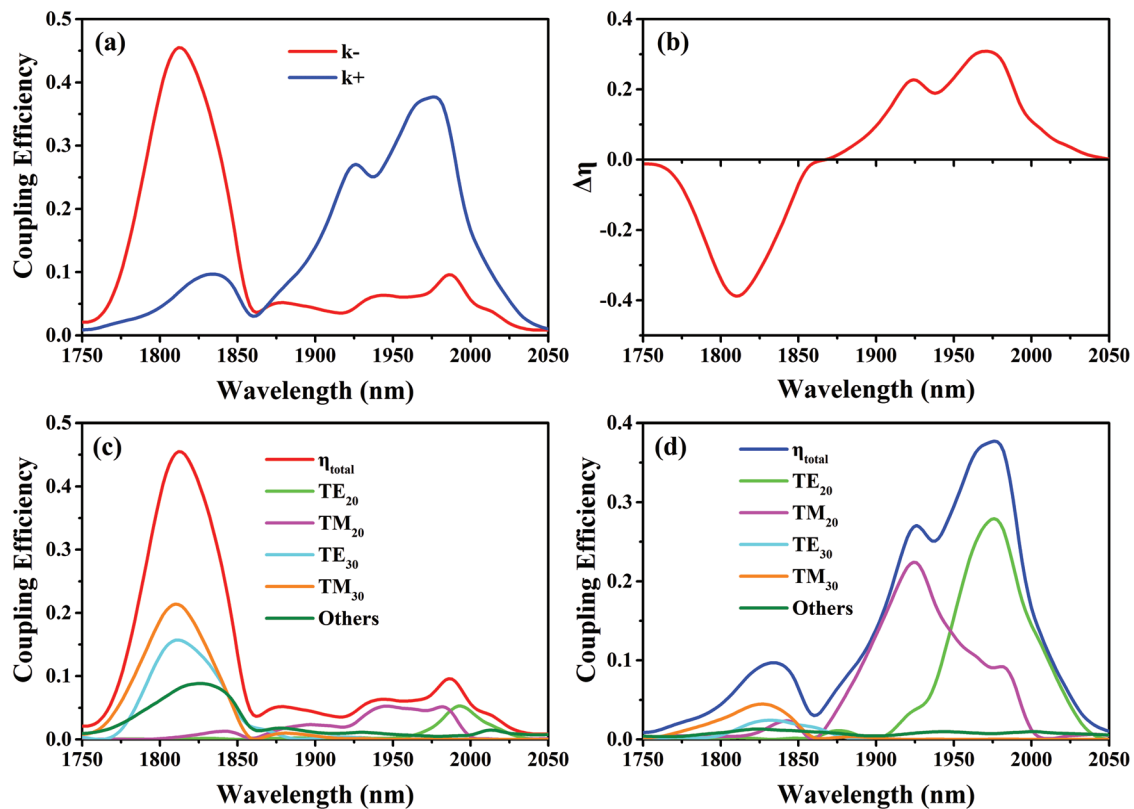


Figure 5. a) Coupling efficiency spectra toward different sides of the waveguide for the spin-selective wavelength demultiplexing device for RCP incidence. The waveguide width is 3000 nm and its thickness is 800 nm. b) Coupling efficiency difference $\Delta\eta$ between the two sides of the waveguide. c) Mode decomposition of the coupling efficiency spectra toward the $-x$ direction. d) Mode decomposition of the coupling efficiency spectra toward the $+x$ direction.

The light that propagates toward the $-x$ direction at about 1810 nm is composed mainly of the TE_{30} and TM_{30} modes. However, for the light that propagates toward the $+x$ direction at about 1926 and 1970 nm, the waveguide modes are mainly composed of the TM_{20} and TE_{20} modes, respectively. With increasing waveguide width, the effective refractive indices of the waveguide modes at each wavelength will increase. Consequently, the phase-matching condition will be satisfied at longer wavelengths. Therefore, the phase-matching condition for the spin-selective directional coupler cannot be applied directly to the wavelength demultiplexing device. Compared with the spin-selective directional coupler, the TE_{20} and TM_{20} modes will be redshifted into the range 1900–2000 nm, as shown in Figure 5d.

To further study the directional excited waveguide modes, we plot the electric field amplitude distribution $|\vec{E}|$ in the x - y plane bisecting the waveguide for RCP incidence at 1810 and 1970 nm in Figure 6a and 6c, respectively. It can be seen that a waveguide mode with four antinodes along y -axis is excited and routed to the $-x$ direction at 1810 nm, which is a mixed mode comprising mainly the TE_{30} and TM_{30} modes. At 1970 nm, a waveguide mode that has three antinodes along the y -axis is excited and routed to the $+x$ direction, which is a mixed mode that consists mainly of the TE_{20} and TM_{20} modes. To demonstrate the origin of the spin-selective wavelength demultiplexing, we plot the Stokes parameters S_3/S_0 for the mode fields in the x - y plane bisecting the waveguide for RCP

incidence at 1810 and 1970 nm in Figure 6b and d, respectively. It can be seen that the distributions of the chiral points at the two wavelengths are different. At 1810 nm, the Stokes parameters S_3/S_0 have four maximum values and four minimum values along the y -axis. The three rows of antenna arrays were located approximately in the blue region (left-handed rotation region) of the mode that propagates toward the $-x$ direction and the red region (right-handed rotation region) of the mode that propagates toward the $+x$ direction. Given that the cross-polarized light converted by the nanoantenna arrays is LCP light, the excited waveguide mode will propagate toward the $-x$ direction (Figure 6a). At 1970 nm, the Stokes parameters S_3/S_0 have three maximum values and three minimum values along the y -axis. Similar to the case discussed above, incident light will be converted to the mode whose local in-plane polarization around the antenna arrays is opposite to the incident polarization. That is to say, the incident light will be routed to the $+x$ direction (Figure 6c). It should be noted that if the chirality of the incident light was reversed, the light flow in the waveguide would be flipped to the opposite direction. Thus, this device can also be considered a wavelength-selective spin demultiplexing device.

In conclusion, we propose and demonstrate a novel approach for the design of a spin-selective directional coupler and spin-selective wavelength demultiplexing device by integrating an all-dielectric metasurface into a silicon nitride waveguide.

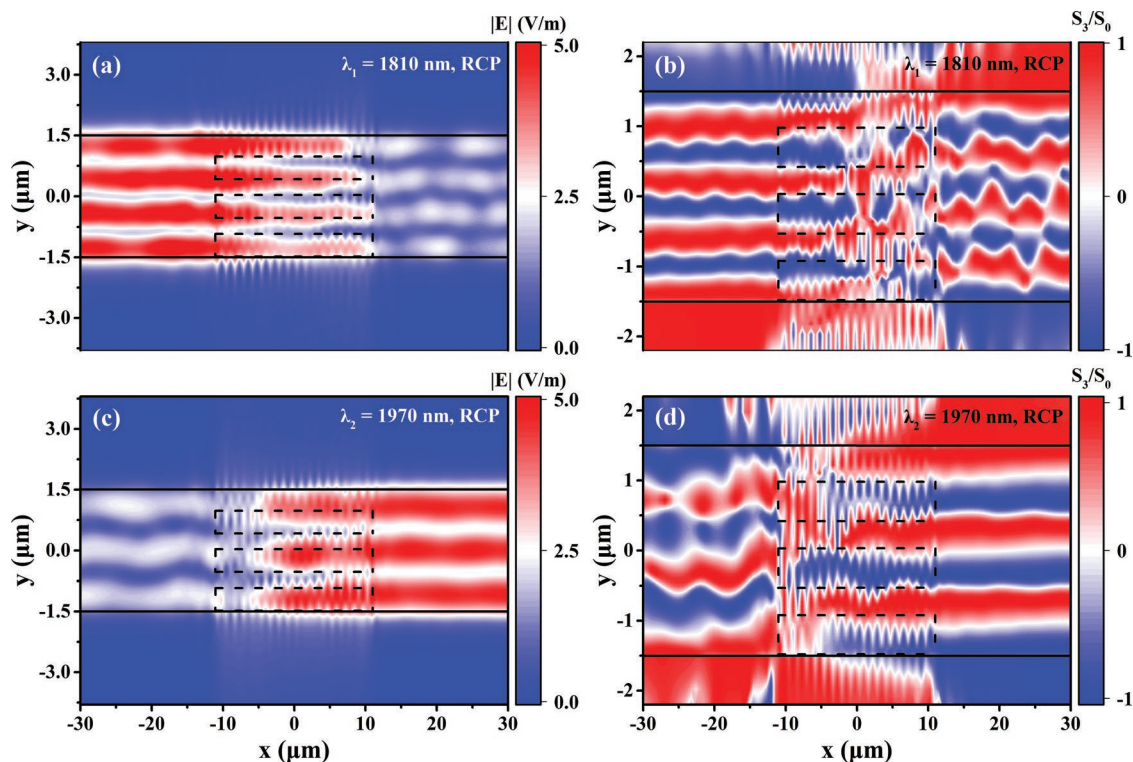


Figure 6. a) Electric field amplitude distribution $|\vec{E}|$ and b) Stokes parameter S_3/S_0 in the x - y plane bisecting the waveguide for RCP incidence at 1810 nm. c) Electric field amplitude distribution $|\vec{E}|$ and d) Stokes parameter S_3/S_0 in the x - y plane bisecting the waveguide for RCP incidence at 1970 nm.

The phase gradients provided by the metasurface are used to satisfy the phase-matching condition. When nanoantennas are placed at the chiral points of the waveguide, the coupling of the electromagnetic field scattered by the nanoantennas and the mode field inside the waveguide lead to spin-selective directional propagation. The propagation direction of the excited waveguide mode can be controlled easily by the spin and wavelength of the incident light. In addition, the coupling efficiency, peak width, and mode type can also be tailored easily by adjusting the geometric parameters of the waveguide and antenna arrays, making it more adaptable to potential applications. According to the phase-matching condition $\left(n_{\text{eff}} = \frac{\lambda}{2P}\right)$ between the coupler and the waveguide mode, the working wavelengths can be tuned easily across a wide range of the near-infrared by tailoring parameter P and the effective refractive index n_{eff} of the waveguide mode. Specifically, we can decrease the size of the waveguide or the distance between the nanopillars along the x -axis to tune the spin-selective directional coupler to telecom wavelength bands. It should be noted that the dimensions of the Si pillars should also be adjusted to ensure reasonably high polarization conversion efficiency in this wavelength band.

The proposed spin-selective and wavelength-selective demultiplexing technique provides a novel approach to encode information with polarization and wavelength simultaneously. Recently, it has been demonstrated that waveguides and metasurfaces can both generate and manipulate optical vortex states.^[34–37] Thus, using waveguide-integrated metasurfaces

and the spin–momentum locking effect, the SAM and orbital angular momentum of photons are expected to be manipulated simultaneously in future photonic integrated circuits. Furthermore, these devices could be integrated with quantum dots to explore chiral quantum optics or be applied as components in integrated quantum optic applications.^[1,2,4,22,38]

Acknowledgements

This work was supported by the National Key Research and Development Program of China (Grant Nos. 2017YFA0303800 and 2016YFA0301102), the National Natural Science Foundation of China (Grant Nos. 91856101, 11574163, and 11774186), the Natural Science Foundation of Tianjin (16JCQNJC01700), and 111 Project (B07013).

Conflict of Interest

The authors declare no conflict of interest.

Keywords

metasurfaces, spin-selective directional coupling, waveguides, wavelength demultiplexing

Received: September 19, 2018

Revised: November 25, 2018

Published online:

- [1] L.-T. Feng, M. Zhang, Z.-Y. Zhou, M. Li, X. Xiong, L. Yu, B.-S. Shi, G.-P. Guo, D.-X. Dai, X.-F. Ren, G.-C. Guo, *Nat. Commun.* **2016**, *7*, 11985.
- [2] A. Mohanty, M. Zhang, A. Dutt, S. Ramelow, P. Nussenzveig, M. Lipson, *Nat. Commun.* **2017**, *8*, 14010.
- [3] L.-W. Luo, N. Ophir, C. P. Chen, L. H. Gabrielli, C. B. Poitras, K. Bergmen, M. Lipson, *Nat. Commun.* **2014**, *5*, 3069.
- [4] A. Javadi, D. Ding, M. H. Appel, S. Mahmoodian, M. C. Löbl, I. Söllner, R. Schott, C. Papon, T. Pregolato, S. Stobbe, L. Midolo, T. Schröder, A. D. Wieck, A. Ludwig, R. J. Warburton, P. Lodahl, *Nat. Nanotechnol.* **2018**, *13*, 398.
- [5] A. Y. Piggott, J. Lu, K. G. Lagoudakis, J. Petykiewicz, T. M. Babinec, J. Vučković, *Nat. Photonics* **2015**, *9*, 374.
- [6] B. Shen, P. Wang, R. Polson, R. Menon, *Nat. Photonics* **2015**, *9*, 378.
- [7] B. Stern, X. Zhu, C. P. Chen, L. D. Tzuan, J. Cardenas, K. Bergman, M. Lipson, *Optica* **2015**, *2*, 530.
- [8] J. Wang, S. He, D. Dai, *Laser Photonics Rev.* **2014**, *8*, L18.
- [9] D. Dai, C. Li, S. Wang, H. Wu, Y. Shi, Z. Wu, S. Gao, T. Dai, H. Yu, H.-K. Tsang, *Laser Photonics Rev.* **2018**, *12*, 1700109.
- [10] D. Dai, J. Wang, S. Chen, S. Wang, S. He, *Laser Photonics Rev.* **2015**, *9*, 339.
- [11] S. J. Kim, J.-H. Kang, M. Mutlu, J. Park, W. Park, K. E. Goodson, R. Sinclair, S. Fan, P. G. Kik, M. L. Brongersma, *Nat. Commun.* **2018**, *9*, 316.
- [12] Y. Li, J. Zhang, D. Huang, H. Sun, F. Fan, J. Feng, Z. Wang, C. Z. Ning, *Nat. Nanotechnol.* **2017**, *12*, 987.
- [13] F. B. Arango, A. Kwadrin, A. F. Koenderink, *ACS Nano* **2012**, *6*, 10156.
- [14] R. Guo, M. Decker, I. Staude, D. N. Neshev, Y. S. Kivshar, *Appl. Phys. Lett.* **2014**, *105*, 053114.
- [15] D. Vercautse, P. Neutens, L. Lagae, N. Verellen, P. V. Dorpe, *ACS Photonics* **2017**, *4*, 1398.
- [16] R. Guo, M. Decker, F. Setzpfandt, X. Gai, D. Y. Choi, R. Kiselev, A. Chipouline, I. Staude, T. Pertsch, D. N. Neshev, Y. S. Kivshar, *Sci. Adv.* **2017**, *3*, e1700007.
- [17] S. Chen, Z. Li, Y. Zhang, H. Cheng, J. Tian, *Adv. Opt. Mater.* **2018**, *6*, 1800104.
- [18] Z. Li, M.-H. Kim, C. Wang, Z. Han, S. Shrestha, A. C. Overvig, M. Lu, A. Stein, A. M. Agarwal, M. Lončar, N. Yu, *Nat. Nanotechnol.* **2017**, *12*, 675.
- [19] C. Wang, Z. Li, M.-H. Kim, X. Xiong, X.-F. Ren, G.-C. Guo, N. Yu, M. Lončar, *Nat. Commun.* **2017**, *8*, 2908.
- [20] C. Gong, J. Zhang, S. He, *Opt. Lett.* **2017**, *42*, 5098.
- [21] J. Petersen, J. Volz, A. Rauschenbeutel, *Science* **2014**, *346*, 67.
- [22] R. J. Coles, D. M. Price, J. E. Dixon, B. Royall, E. Clarke, P. Kok, M. S. Skolnick, A. M. Fox, M. N. Makhonin, *Nat. Commun.* **2016**, *7*, 11183.
- [23] L. Fang, J. Wang, *Phys. Rev. A* **2017**, *95*, 053827.
- [24] A. Espinosa-Soria, A. Martinez, *IEEE Photonics Technol. Lett.* **2016**, *28*, 1561.
- [25] S. Luo, L. He, M. Li, *Nat. Commun.* **2017**, *8*, 2141.
- [26] T. V. Mechelen, Z. Jacob, *Optica* **2016**, *3*, 118.
- [27] M. F. Picardi, A. V. Zayats, F. J. Rodríguez-Fortuño, *Phys. Rev. Lett.* **2018**, *120*, 117402.
- [28] M. F. Picardi, A. Manjavacas, A. V. Zayats, F. J. Rodríguez-Fortuño, *Phys. Rev. B* **2017**, *95*, 245416.
- [29] A. Pors, S. I. Bozhevolnyi, *Phys. Rev. Appl.* **2016**, *5*, 064015.
- [30] Y. Guo, M. Pu, X. Li, X. Ma, S. Song, Z. Zhao, X. Luo, *IEEE J. Sel. Top. Quantum Electron.* **2018**, *24*, 1.
- [31] *COMSOL Multiphysics User's Guide, Version 4.3*, Comsol AB, Burlington, MA, USA **2012**.
- [32] E. D. Palik (Ed.), *Handbook of Optical Constants of Solids*, Academic Press, San Diego, CA, USA **1998**.
- [33] K. Luke, Y. Okawachi, M. R. E. Lamont, A. L. Gaeta, M. Lipson, *Opt. Lett.* **2015**, *40*, 4823.
- [34] A. Liu, C.-L. Zou, X. Ren, Q. Wang, G.-C. Guo, *Appl. Phys. Lett.* **2016**, *108*, 181103.
- [35] S. Zhang, J. Wang, *Opt. Express* **2017**, *25*, 18492.
- [36] F. Yue, D. Wen, C. Zhang, B. D. Gerardot, W. Wang, S. Zhang, X. Chen, *Adv. Mater.* **2017**, *29*, 1603838.
- [37] C. Zhang, F. Yue, D. Wen, M. Chen, Z. Zhang, W. Wang, X. Chen, *ACS Photonics* **2017**, *4*, 1906.
- [38] P. Lodahl, S. Mahmoodian, S. Stobbe, A. Rauschenbeutel, P. Schneeweiss, J. Volz, H. Pichler, P. Zoller, *Nature* **2017**, *541*, 473.